

Natural Frequency Dependency of Magneto-Mechanical Resonators on Magnet Distance

Jonas Faltinath,^{1, 2,*} Fabian Mohn,^{1, 2} Flynn Foerger,^{1, 2} Martin Möddel,^{1, 2} and Tobias Knopp^{1, 2, 3}

¹Section for Biomedical Imaging, University Medical Center Hamburg-Eppendorf, Hamburg, Germany

²Institute for Biomedical Imaging, Hamburg University of Technology, Hamburg, Germany

³Fraunhofer Research Institution for Individualized and Cell-Based Medical Engineering IMTE, Lübeck, Germany

(Dated: March 7, 2025)

The precise derivation of physical quantities like temperature or pressure at arbitrary locations is useful in numerous contexts, e.g. medical procedures or industrial process engineering. The novel sensor technology of magneto-mechanical resonators (MMR), based on the interaction of a rotor and stator permanent magnet, allows for the combined tracking of the sensor position and orientation while simultaneously sensing an external measurand. Thereby, the quantity is coupled to the torsional oscillation frequency, e.g. by varying the magnet distance. In this paper, we analyze the (deflection angle-independent) natural frequency dependency of MMR sensors on the rotor-stator distance, and evaluate the performance of theoretical models. The presented sensors incorporate magnets of spherical and/or cylindrical geometry. We find the distance-frequency relationship to be well described by an adapted dipole model accounting for material and manufacturing uncertainties. Their combined effect can be compensated by an adjustment of a single parameter which drives the median model deviation generally below 0.2 %. Our depicted methods and results are important for the design and calibration process of new sensor types utilizing the MMR technique.

I. INTRODUCTION

Passive and wireless sensors have many advantages over their wired counterparts in certain applications such as condition and structural monitoring, process control, and healthcare [1–3]. In particular, they can play a crucial role for the accurate determination of the position and orientation of medical instruments which is essential for procedures such as surgery, endoscopy, and vascular interventions [4–6]. Also, the performance evaluation of (bio-)chemical reactions in industrial reactors is sensitive to precise knowledge about spatial parameters [7, 8]. The incorporation of small permanent magnets in a localization and measurement device is an active area of research [9, 10] and the recently introduced magneto-mechanical resonator (MMR) platform [11, 12] is suited for miniaturization and could be applicable in the stated contexts.

The setup proposed in [11] has the advantage to allow the determination of all six spatial degrees of freedom of a sensor (tracking) and the simultaneous measurement of additional physical parameters such as temperature and pressure (sensing). As outlined in Fig. 1, the design of the MMR sensor includes two permanent magnets with antiparallel magnetic moments. The stator magnet is attached to the housing, whereas the rotor is suspended by a filament, able to rotate around the filament axis. The fundamental principle of the MMR is similar to a torsional pendulum where the rotor performs damped oscillations around the equilibrium position after initial deflection by an external magnetic field. The necessary restoring torque is supplied by the magnetic interaction

with the stator. In analogy to inductor-capacitor (LC) passive wireless sensors, the signal of the MMR sensor can be excited and detected via induction [3, 13].

To achieve sensing capabilities with an MMR, an external parameter like the environment pressure or temperature needs to be coupled to the oscillator. In the simplest approach, this can be realized by changing the magnet distance with e.g. a compressible housing [11, 14] or thermally deforming filament [12]. This results in a parameter-dependent alteration of the restoring torque

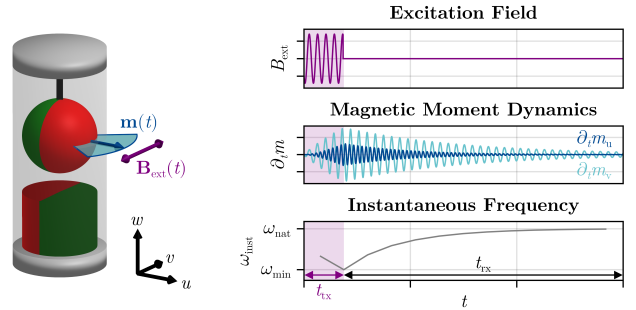


FIG. 1. Left: Fundamental components of an MMR. The filament keeps the rotor (upper magnet) at a defined distance to the stator (lower magnet). An external magnetic field $B_{\text{ext}}(t)$ can deflect the rotor's magnetic moment $\mathbf{m}(t)$ from its equilibrium position. Right: Typical MMR measurement frame consisting of excitation (t_{tx} , purple shading) and receive window (t_{rx}). The components $\partial_t m_{u,v}(t)$ are proportional to the induction signal in a coil. Note that due to the projection, we find the torsional frequency only in v -direction (light blue) but twice of it in u -direction (dark blue). For oscillations with a high quality factor, the instantaneous angular frequency ω_{inst} of this non-linear oscillator approaches the natural angular frequency ω_{nat} in the limit of vanishing deflection amplitude.

* Contact author: j.faltinath@uke.de

and thus of the measurable frequency which we investigate in this study. We note that non-linear oscillators show an additional dynamic coupling between the deflection angle and the instantaneous oscillation frequency, as illustrated in Fig. 1. To guarantee well-defined MMR sensing, we introduce the deflection angle-independent natural frequency. Oscillators with high quality factor converge towards this frequency for infinitesimally small deflection amplitude.

In this paper, we separate our analysis from any external physical quantity making our results applicable for sensors independent of the precise origin of the distance change. Our measurements are performed on MMRs, composed of magnetic spheres and cylinders, specially engineered to cover a wide range of magnet-to-magnet distances. We compare these data sets with the frequency prediction of a fully determined dipole model and phenomenological models to gain an understanding of underlying deviations. The findings from this paper are a generalized and methodically substantially optimized extension of preliminary work published as a conference proceedings paper [15].

II. MATERIALS AND METHODS

A. Sensor Design

In this study, we compare three MMRs that differ in the choice of the magnet geometry. For the permanent magnets, we select from either spherical (EarthMag GmbH, Germany), or cylindrical (MAGSY GmbH, Germany) neodymium-iron-boron (NdFeB) magnets with uniform diametral magnetization. Their detailed material properties are summarized in Table I. The first MMR consists of two spherical magnets, the second of two cylinders and the third is built with a spherical rotor and a cylindrical stator. In the following, we refer to these sensors as Sphere-, Cylinder- and Hybrid-MMR, respectively (see Fig. 2(c) for images). The specialized design of our sensor housings features a mechanism to precisely adjust the center-to-center distance between the magnets allowing us to measure an isolated magnet distance series on an otherwise unchanged system.

Our cuboidal, non-magnetic housing design is based on four 3D-printed components which are detailed in Fig. 2(a)-(b). The continuous adjustment screw

TABLE I. Manufacturer specifications of the permanent magnets utilized for MMR construction. The magnets of spherical or cylindrical geometry have a similar footprint but differ in their stated degree of magnetization.

Geometry	Grade	Remanence	Diameter	Height	Mass
Spherical	N40	1.26 – 1.29 T	4 mm	–	0.35 g
Cylindrical	N35	1.17 – 1.24 T	4 mm	4 mm	0.38 g

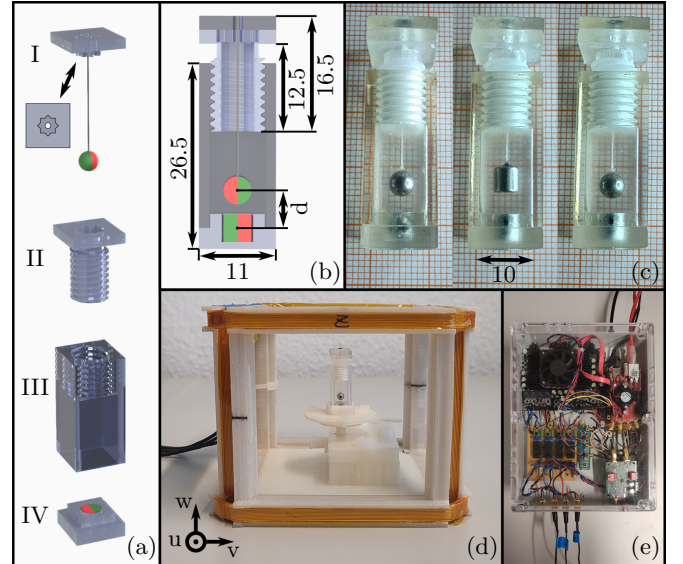


FIG. 2. Components of the measurement setup (all lengths in units of mm). (a) Exploded-view drawing showing the four-part concept of the adjustable 3D-printed MMR housing. It consists of the filament anchor (I) with an octagram-shaped stamp (inset), the attached filament and rotor magnet, the adjustment screw (II) with M8 thread, the carrier element (III) and the stator mount (IV). (b) Cross section of the housing. By rotation of the screw, the center-to-center distance d between rotor and stator can be changed (1.25 mm per full rotation). Simultaneous raising of the anchor prevents filament twisting. (c) Images of the Sphere-, Cylinder- and Hybrid-MMR (from left to right). (d) 3D coil arrangement aligned with the MMR coordinate system from Fig. 1 and vertical translation mount for sensor centering. (e) Image of the three-channel transmit-receive chain electronics for generating the excitation signal and for induction signal processing [16].

(Fig. 2(a) II) is the central element for setting distances. Its lower end can be connected to the carrier element (Fig. 2(a) III) via a machined M8 thread that allows a translational motion of 1.25 mm per full rotation. To enhance transparency of the housing, the outer facets of the carrier element are polished and finished with clear lacquer. The sub-mm thin filament is made of ultra-high-molecular-weight polyethylene. With instant adhesive gel, it is fixed only to the rotor magnet and inside a through hole of the filament anchor (Fig. 2(a) I). Finally, the stator mount (Fig. 2(a) IV) completes the housing.

To avoid a changing contribution of the suspension to the restoring torque when the distance is adjusted, our design minimizes filament twisting by having no permanent connection with the rotatable adjustment screw. Instead, the anchor (along with the filament) is detachable and solely the magnetic attraction of rotor and stator hold the components in place. Hereby, the lower part of the anchor, which forms an octagram-shaped stamp, fits precisely into the corresponding cut-out of the adjustment screw. This design prevents slipping of the anchor during an oscillation but allows to separate the filament

and adjustment screw during a distance change. Defined by the symmetry of the stamp, one eighth of a full rotation represents our smallest distance discretization which does not lead to an increased state of the filament torsion.

B. Excitation and Signal Acquisition

Our MMR measurement sequence consists of a number of repeated frames with identical time span. In accordance with Fig. 1, our implemented transmit-receive (TxRx) system [16] divides each frame again into an excitation window of time t_{tx} , and receive window t_{rx} . For this, we use synchronized electro-mechanical relays to switch between dedicated excitation and receive electronics and to ensure full switching of all the electronic parts, we wait a short time t_{sw} during the transitioning of the windows. The central element for the interaction with the sensor is a cube consisting of three orthogonal pairs of square-shaped coils each acting as a separate inductive excitation and acquisition channel [17]. The corresponding components are presented in Fig. 2(d), (e).

Each of the two lateral coil pairs feature an edge length and a distance of 10 cm whereas the vertical pair has an edge length of 12.8 cm and a distance of 8 cm. Each individual coil is made of 40 turns of thin litz wire consisting of 500 individual copper strands with a diameter of 20 μm . Biot-Savart simulations show that within a volume element of 1 cm^3 around the center of the setup, the expected magnetic field deviation is less than 1.5 % and field strengths exceeding $B_{ext} = 40 \mu\text{T}$ can be realized.

We control the measurement sequence by a computer connected to a system-on-a-chip (STEMlab 125-14, Red Pitaya d.o.o., Slovenia) that acts as our digital-to-analog converter (DAC) during the excitation window and as analog-to-digital converter (ADC) during the receive window. It allows us to freely tune the TxRx timings (t_{tx}, t_{sw}, t_{rx}). During the excitation window, we deflect the MMR rotor from its equilibrium position. To this end, a sinusoidal DAC voltage output is amplified by a four-channel class-D amplifier (Sure Electronics Co., Ltd., Malaysia) which supplies the coils with current via a low-impedance circuit. The system allows for dynamic adaptions of the excitation signal amplitude, frequency and phase of each channel. In our setup, we find a linear behavior between DAC output and coil current amplitude for frequencies up to $\sim 400 \text{ Hz}$. In the receive window, we measure the induction signals created by the oscillating magnetic moment of the MMR rotor. Hence, the relays switch the coils into a high-impedance circuit. For analog-to-digital conversion, we amplify the acquired voltage with an operational amplifier by a factor of ~ 100 .

Currently, we do not use a control ensuring an in-phase relation between residual motion of the oscillator at the end of a frame and the newly applied excitation signal of the next frame. However, in parallel to signal acquisition, we perform a real-time fast Fourier transform (FFT) for an active excitation frequency control. Starting with

an initial guess for the first frame, the Fourier spectrum determines the set frequency for the excitation window of each immediately following frame. The corresponding value is not to be confused with the natural frequency which is independent on the specific rotor deflection angle and derived solely during post-processing (see section II E).

C. Experimental Execution

The primary objective of this paper is to study the relation between MMR rotor-stator distance and its natural oscillation frequency. For each of the three MMRs, we start the measurement process by adjusting a center-to-center distance of $d = 10 \text{ mm}$. With support of the cuboidal format and transparency of the housing, we can verify the magnet distance on a millimeter-scaled graph paper, analogues to Fig. 2(c). Starting from that, any subsequent distance is obtained from the (fractional) number of rotations of the adjustment screw and its pitch, down to the minimum value of $d = 4.2 \text{ mm}$. Before each rotation, we lift the anchor, adhered filament and rotor to prevent twisting of the filament.

As shown in Fig. 2(d), we mount the MMR upright into the cube containing the induction coil pairs by support of a 3D-printed translation- and rotation-mount. With that, we ensure that the rotor is vertically aligned with the center of the homogeneous region for each measured distance. We also rotate the MMR to superimpose coil axes and MMR coordinate system (u, v, w) by utilizing the projection characteristics from Fig. 1. To that end, we adjust the angle such that after excitation we observe the torsional frequency dominantly in one lateral receive channel, and twice its value dominantly in the other. Consequently, the individual channels will be mainly sensitive to respective changes in m_v or m_u . During alignment, the vertical coil pair acts as a verification channel as it does not show any induction if the sensor is positioned correctly. In the measurement sequence, we apply the excitation field only in v -direction which is ideal for efficient MMR stimulation whereas the reception occurs in both lateral directions leading to a two-dimensional vector-valued receive signal $\mathbf{u}(t)$.

For each MMR and distance, our measurement sequence consists of 17 subsequent frames and we fix $t_{sw} = 20 \text{ ms}$. The excitation times and field amplitudes are chosen for each individual sequence between $t_{tx} = 0.5 - 1.0 \text{ s}$ and $B_{ext} = 20 - 30 \mu\text{T}$, respectively, to maximize the initial induction signal amplitude. We choose receive windows between 2 – 30 s to capture nearly complete oscillation signals including the information-carrying decaying part before getting noise-dominated.

D. Equation of Motion

We consider an MMR model where both the rotor and stator are represented as magnetic point dipoles with moments m_r and m_s . In that case, the instantaneous magnetic restoring torque $\tau = m_r B_0 \sin \varphi$ on a rotor that is deflected out of its equilibrium position depends on the magnetic flux density $B_0(m_s)$ produced by the stator and the deflection angle φ [12]. In other designs of general magneto-mechanical oscillators, the suspension of the rotor provides an additional restoring torque [18, 19]. However for our sensors, we neglect any residual contribution of the thin filament and consider the torque as dominated by the magnetic interaction. Finally, we account for frictional losses such that the corresponding equation of motion for φ in free oscillation is equivalent to that of a damped gravitational pendulum and given by

$$\ddot{\varphi} + \frac{\omega_{\text{nat}}}{Q} \dot{\varphi} + \omega_{\text{nat}}^2 \sin \varphi = 0 \quad (1)$$

where ω_{nat} is the natural angular frequency of the resonator and Q is the quality factor affecting the relaxation time $\tau = 2Q/\omega_{\text{nat}}$.

In the small-angle approximation ($\sin \varphi \approx \varphi$), Eq. (1) becomes the equation of motion of a damped harmonic oscillator, which has the explicit solution

$$\varphi(t) = \varphi_{\text{max}} \exp(-t/\tau) \sin(\omega_{\text{inst}} t + \psi_0) \quad (2)$$

where φ_{max} is the maximum deflection angle and ψ_0 is an initial phase at $t = 0$. Only in the case of a high- Q oscillation, the instantaneous angular frequency

$$\omega_{\text{inst}} = \sqrt{1 - \left(\frac{1}{2Q}\right)^2} \omega_{\text{nat}} \quad (3)$$

approaches the natural angular frequency, as illustrated in Fig. 1. In other words, ω_{nat} corresponds to the angular frequency at which an undamped harmonic oscillator would oscillate.

E. Natural Frequency Estimation

To determine the natural oscillation frequency of an MMR, we perform a direct optimization on a physical model taking into account the equation of motion given by Eq. (1). Compared to an isolated analysis of the instantaneous frequency in a late damped-out state, as possible with Eq. (3), our method has the advantage to take the full acquired induction voltage signals $\mathbf{u}(t)$ as an input. Consequently, our estimation performance is independent of Q and not sensitive to varying initial signal amplitudes and corresponding fluctuations in the onset of the small angle approximation.

The received voltage signal for each frame can be modeled by

$$\mathbf{u}(t) = \boldsymbol{\sigma}_v \partial_t \sin(\varphi(t)) + \boldsymbol{\sigma}_u \partial_t \cos(\varphi(t)) \quad (4)$$

where $\boldsymbol{\sigma}_v$ and $\boldsymbol{\sigma}_u$ are amplitude vectors, inherently dependent on m_r and the coil sensitivities. The two terms are explained from the time-dependent magnetic moment projections in either v - or u -direction, for which a general coil has distinct sensitivities. In our alignment, each lateral receive coil pair is predominantly sensitive to one respective component of these two. Additionally to the amplitude vectors, the signal evolution according to Eq. (1) and (4) also depends on the precise values of ω_{nat} , Q and the initial φ_{max} and ψ_0 . For each frame, all these parameters are determined considering a nonlinear least squares (NLLS) approach on the measurement data by means of the Levenberg-Marquardt algorithm (LMA) [20].

F. Frequency Models

To derive an expression for the natural angular frequency in dependence on material parameters, we assign to the modeled point dipoles of rotor and stator (located at their respective center-of-mass) the mechanical properties resulting from their actual extended shape. To comply with the definition for ω_{nat} of section II D, we consider an undamped harmonic (i.e. small-angle approximated) torsional motion with the torsion constant $D = m_r B_0$ and the rotor's moment of inertia I . In this case, we can write $\omega_{\text{nat}} = \sqrt{D/I}$ [12]. For the dipole field produced by the stator, we have $B_0 = \mu_0 m_s / (4\pi d^3)$ where d is the distance between both magnet centers and μ_0 is the vacuum permeability. Thus, the angular natural frequency of this dipole model, labeled as model A, follows as

$$\text{Model A : } \omega_{\text{nat}}^A(d) = \alpha^A d^{-3/2} \quad (5)$$

with

$$\alpha^A := \sqrt{\frac{m_r m_s \mu_0}{4\pi I}}. \quad (6)$$

The material factor α^A depends only on the magnetic and mechanical properties of the sensor components. To obtain this quantity, we consider rotor and stator as geometric objects with uniform magnetization and mass distribution, and take the manufacturer specifications from table I as a reference. Thereby, we use the center value of the stated remanence range to calculate the magnetic moment of the respective magnet. For the moment of inertia, we assume an ideal rotation of the suspended magnet around the axis of rotational symmetry (passing through the center-of-mass) for either a spherical or cylindrical shape with corresponding size and mass.

The frequency prediction of model A is based on various assumptions regarding the construction of our sensors. To allow for a systematic analysis of the contribution of inaccuracies, we derive from model A two additional phenomenological models. The first uncertainty comes from the precision in the knowledge of material

and construction parameters. Both, the obtained rotor and stator magnetization, and the moment of inertia rely on the manufacturer specifications and idealizations in the determination. These parameters contribute to the material factor α^A of model A which is, therefore, chosen as a free parameter in model B. The second uncertainty lies in the validity of the dipole approximation for our spatially extended magnets. The assumption of point-like magnets provides an exact description of the interaction only for homogeneously magnetized spheres [21]. In contrast and inherently as a result of their geometry, the produced field of cylinders differs from a dipole field [22] such that the dipole approximation is matched just in the case of a large separation between the magnets. However, our sensors are subject to magnet edge-to-edge distances on the order of the magnet size and below, yielding the need for an accurate evaluation of near-field deviations. Consequently in model C, we allow for the additional adaptation of the polynomial degree of the spatial field profile B_0 . In summary, these models are described by

$$\text{Model B : } \omega_{\text{nat}}^B(d, \alpha^B) = \alpha^B d^{-3/2}, \quad (7)$$

$$\text{Model C : } \omega_{\text{nat}}^C(d, \alpha^C, \gamma^C) = \alpha^C d^{-\gamma^C/2}, \quad (8)$$

with free parameters α^B , α^C and γ^C . These are optimized for each model on the measured frequency values employing a weighted NLLS fit minimizing the sum of the squared relative residuals using the LMA. We quantify the scale of adaption compared to the fully determined model A by computation of the relative parameter deviation $\Delta\alpha = (\alpha^{B,C} - \alpha^A)/\alpha^A$ and $\Delta\gamma = (\gamma^C - \gamma^A)/\gamma^A$ with $\gamma^A = 3$.

To evaluate the agreement between the established model $M \in \{A, B, C\}$ and the measurement data, we apply an analysis of the relative residuals defined by

$$\varepsilon^M(d) = \frac{\omega_{\text{nat}}^M(d) - \omega_{\text{nat}}^{\text{meas}}(d)}{\omega_{\text{nat}}^{\text{meas}}(d)} \quad (9)$$

for each distance. Thereby, $\omega_{\text{nat}}^{\text{meas}}$ is the natural angular frequency obtained from averaging all frames from a single measurement sequence.

III. RESULTS

Our results for the relation between magnet distance and natural frequency are summarized in Fig. 3. In the left part, we show the measured and modeled frequency values for each of the three constructed MMRs. Within a single measurement sequence, we observe large frame-to-frame variations in the initial deflection amplitude, with the largest range spanning $\varphi_{\text{max}} = 9.6 - 31.8^\circ$. Nonetheless, there is a strong reproducibility in the determination of the natural frequency yielding statistical errors on the mean generally smaller than 0.05 %. Depending on the measurement configuration, we find sequence-averaged quality factors ranging from $Q = 186 - 14\,052$. The

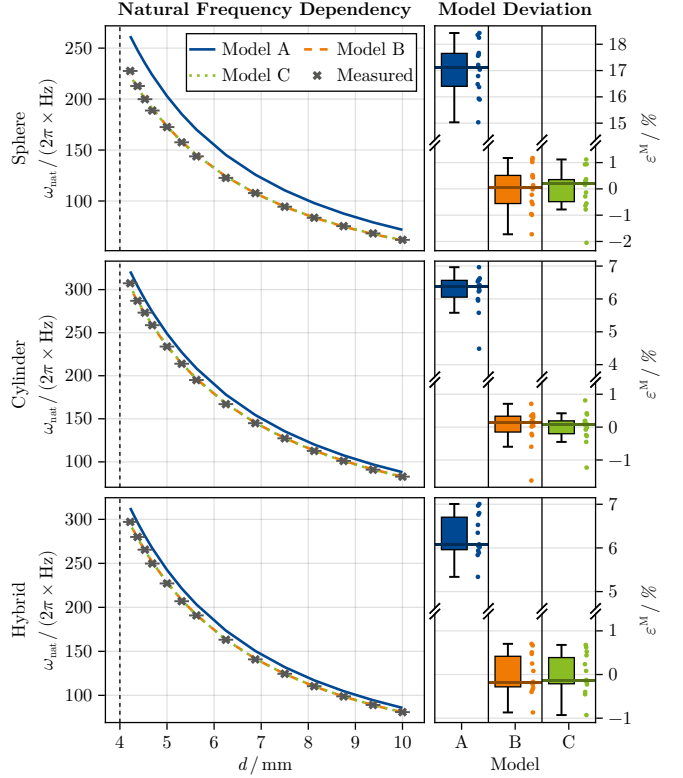


FIG. 3. Left: Measured mean natural angular frequencies ω_{nat} in units of Hz for different magnet center-to-center distances d in comparison to predictions from models A, B, and C. We show the data sets for the sensors labeled as Sphere-(first row), Cylinder- (second row) and Hybrid-MMR (last row). Each frequency value is obtained from averaging 17 subsequent frames where we generally find statistical errors on the mean smaller than the marker size. The horizontal bars show the experimental uncertainty in the determination of d . The black dashed line marks the contact point between rotor and stator. Right: Box plots combining the model deviations ε^M according to Eq. (9) for all measured distances. Each dot represents a sequence-averaged data point, the box limits are defined by the lower and upper quartile, and the whisker expands the interquartile range by a maximum factor of 1.5. The horizontal lines mark the median deviation. Note the break in the vertical axes for improved visibility.

quality factors show frame-to-frame fluctuations during a measurement sequence, where the maximum standard deviation of the mean lies at 16.2 %. We note that the magnet distance and Q do not exhibit a simple scaling behavior in our measurements.

In general, the oscillation frequency is increasing with decreasing center-to-center distance for all investigated sensors. The measured frequencies span a range of 61.9 – 227.6 Hz for the Sphere-MMR, 82.8 – 307.3 Hz for the Cylinder-MMR and 81.0 – 297.1 Hz for the Hybrid-MMR. For each model and sensor, we show the statistics of the distance-combined ε^M as box plots on the right side of Fig. 3. In addition, we evaluate in table II the degree of adaption of the free parameters in the phe-

nomenological models compared to model A and specify the overall model performances. In comparison to our measurements, the dipole model A predicts higher frequencies for all sensors with the strongest discrepancy for the sensor with spherical rotor and stator. We observe that the material factors α^B are generally reduced compared to α^A with the largest percentage adjustment again for the Sphere-MMR. In model B, the absolute median model deviations can be brought to a similar level below 0.2 % for all three MMRs with a maximum interquartile range of 1.1 %. The $\tilde{\varepsilon}^M$ from the least restrictive model C are comparable to these values. Regarding to the dipole value, the exponent γ^C needs to be only slightly adjusted by not more than 0.7 %.

TABLE II. Comparison of model performances. For the three sensors, we present the median of the distance-combined model deviation distribution of Fig. 3, denoted by $\tilde{\varepsilon}^M$. We also show the relative deviations $\Delta\alpha$ and $\Delta\gamma$ for the optimized free parameters in model B (α^B) and C (α^C , γ^C) compared to the values of model A.

MMR	Model A $\tilde{\varepsilon}^A$ /%	Model B		Model C		
		$\Delta\alpha$ /%	$\tilde{\varepsilon}^B$ /%	$\Delta\alpha$ /%	$\Delta\gamma$ /%	$\tilde{\varepsilon}^C$ /%
Sphere	17.1	-14.6	0.1	-10.8	-0.6	0.2
Cylinder	6.4	-5.8	0.1	-10.7	0.7	0.1
Hybrid	6.1	-5.9	-0.2	-5.1	-0.1	-0.1

IV. DISCUSSION

The presented study supplies valuable insights into the characteristics of MMR signals and their appropriate modeling. In particular, we define the natural oscillation frequency as an important parameter for sensing applications and provide quantitative statements on its scaling with the magnet distance for sensors featuring different rotor and stator geometries.

Our method to obtain the natural frequency from an induction signal proves to give high-precision results with negligible statistical error. Notably, our procedure is not sensitive to our setup limitation of frame-variant initial deflection amplitudes originating from the absence of a corresponding active excitation signal phase and amplitude control, even for variations as large as 22°. All the investigated sensors operate in the limit of low-damped oscillators with $Q > 100$, however, we observe a strong variability of this quantity with no obvious trend in dependence on the magnet choice and distance. A detailed analysis on the origin of the underlying relationship is beyond the scope of this study. Nevertheless, we account for the corresponding individual damping time-scales to capture as much information about the dynamics as possible explaining the large range of receive windows in our experiment. Since our optimization is performed directly on the equation of motion, our method provides,

consequently, a very accurate estimate of the natural frequency.

The general trend of an increase in the natural frequency when the magnet distance is reduced stems from the rise in the magnetic field strength and corresponding enhancement of the restoring torque on the rotor. Qualitatively, this behavior is well described by all presented models. However, we have a systematic discrepancy between measurements and model A towards higher frequency predictions with median model deviations of more than 6 %, for the Sphere-MMR even reaching 17.1 %. We note that model A is fully determined by the best available knowledge of idealized material and geometrical properties. In contrast, the models B and C both drive the model error close to zero. Compared to the dipole value, our method systematically reduces the material factors $\alpha^{B,C}$ for all sensors, up to in maximum -14.6 % for the Sphere-MMR in model B. There is no substantial further improvement in the model performances when transitioning to model C with additional free parameter. Consequently, the observed minor optimizations (well below 1 %) in γ^C compared to the dipole value can be attributed to overfitting on the measurement data and have no physical significance. In summary, model A is not sufficient to describe the observations, whereas model B outperforms model C because of its reduced complexity. We note that due to the data-driven nature of the proposed model, small (systematic) deviations with the measurements still persist and ultimately limit the estimation accuracy and sensor sensitivity.

Our findings highlight the importance of an accurate material factor to reach consistency with the acquired data. Furthermore from the analysis of the exponent γ^C , which is a measure for the validity of the dipole approximation, we emphasize that there is no indication to assume a magnetic field scaling other than that of a dipole field to describe the magnetic interaction of rotor and stator and to predict the corresponding natural frequency. While this is expected for spheres [21], it contrasts with the reported behavior for cylindrical magnets where a separation-dependent disagreement between the actual and a dipole field on the order of a few percent is described [22]. However, we note that [22] provides an isolated view on the scaling of the field profile of a single extended magnet which is not directly transferable to our results based on the interaction of two magnets.

Any residual offsets originating from that seem to be mainly absorbed into the adequate adaption of the material factor. In addition to that, the single parameter α^B accounts non-specifically for uncertainties of the magnet magnetization and the rotor's moment of inertia compared to the assumptions of model A where the material factor is overestimated. There are various aspects in our constructed MMRs that can contribute to such deviations. On the one hand, manufacturing discrepancies of the stated magnetization for the permanent magnets could occur. We note that for all sensors, a simple shift of the assumed remanence inside the limits of the man-

ufacturing range from table I is not sufficient to push the error of model A to the same level as with model B. On the other hand, the moment of inertia is very sensitive to the precise mass density distribution and rotational axis of the oscillating object. There are influences from e.g. a small relative tilt of the magnets and the exact amount, shape and position of glue at the bonding point of rotor and filament. These contributions are not captured in model A and represent factors to increase I which, according to Eq. (5) and (6), leads to smaller natural frequencies compared to the expectations. We remark that due to the spherical symmetry, which makes precise mounting more challenging, both spherical rotors and stators are more likely a subject to such manufacturing deficits than cylinders of the same size. This is in reasonable agreement with having the largest deviation between the Sphere-MMR and the fully determined model.

Material and manufacturing uncertainties are very specific to individual sensors and difficult to predict. However, a larger size, mass and higher degree of magnetization of the permanent magnets reduces the relative influence of irregularities. In particular with view on that, our results can be considered as consistent with the preliminary findings from [15].

V. CONCLUSIONS AND OUTLOOK

We performed the first systematic experimental study investigating the dependency between the natural MMR frequency and the rotor-stator distance. Notably, we were able to show that the mere presence of manufacturing uncertainties does not lead to an unpredictable sensor response but can be readily accounted for by the

adjustment of a single parameter α^B in a magnetic point dipole based model. Consequently, our established model can capture the scaling of the natural frequency with the magnet center-to-center distance, independently of the rotor and stator geometry, given that a good estimate for this material factor is known.

Our presented method is of value since the usage of MMRs as an applicable sensor is subject to the necessity of ongoing miniaturization, corresponding rising construction difficulty, and susceptibility to errors. Instead of performing a time-consuming precision analysis on all material parameters of the mechanical oscillator, we propose the transition to a few-point calibration approach in combination with a phenomenological model. We note that application-oriented sensors are served to measure an external parameter and, therefore, include a coupling mechanism between measurand and distance. This application-specific element might involve additional non-linearities (e.g. the deflection of a membrane for pressure sensing [14]) which were excluded in our study. Correspondingly, there is the need to generalize our model to describe the natural frequency in dependence on the measurand. In case, there is an independent model for the relation between external parameter and distance, both can be easily combined. We also highlight the performance of our method to obtain the natural frequency which has proven to be insensitive to the quality of an excitation. This is an advantage since there is no need to achieve constant rotator deflection angles during sensing.

In conclusion, our findings can guide the design and characterization process of application-oriented sensors. They represent an important step towards the fully quantitative sensing of e.g. temperature, pressure or other quantities based on magneto-mechanical resonance.

-
- [1] R. Bogue, Wireless sensors: a review of technologies, products and applications, *Sensor Review* **30**, 285 (2010).
 - [2] D. He, Y. Cui, F. Ming, and W. Wu, Advancements in passive wireless sensors, materials, devices, and applications, *Sensors* **23** (2023).
 - [3] Q.-A. Huang, L. Dong, and L.-F. Wang, Lc passive wireless sensors toward a wireless sensing platform: Status, prospects, and challenges, *Journal of Microelectromechanical Systems* **25**, 822 (2016).
 - [4] A. Ramadani, M. Bui, T. Wendler, H. Schunkert, P. Ewert, and N. Navab, A survey of catheter tracking concepts and methodologies, *Medical Image Analysis* **82**, 102584 (2022).
 - [5] J. Kaesmacher, J. Gralla, P. J. Mosimann, F. Zibold, M. R. Heldner, E. Piechowiak, T. Dobrocky, M. Arnold, U. Fischer, and P. Mordasini, Reasons for reperfusion failures in stent-retriever-based thrombectomy: registry analysis and proposal of a classification system, *American Journal of Neuroradiology* **39**, 1848 (2018).
 - [6] F. J. A. Montè Alverne, F. O. Lima, F. de Araújo Rocha, D. de Almeida Bandeira, A. F. de Lucena, H. C. Silva, J. S. Lee, and R. G. Nogueira, Unfavorable vascular anatomy during endovascular treatment of stroke: challenges and bailout strategies, *Journal of Stroke* **22**, 185 (2020).
 - [7] D. E. Mears, Tests for transport limitations in experimental catalytic reactors, *Industrial & Engineering Chemistry Process Design and Development* **10**, 541 (1971).
 - [8] J. Shabanian and J. Chaouki, Effects of temperature, pressure, and interparticle forces on the hydrodynamics of a gas-solid fluidized bed, *Chemical Engineering Journal* **313**, 580 (2017).
 - [9] F. Fischer, C. Gletter, M. Jeong, and T. Qiu, Magneto-oscillatory localization for small-scale robots, *npj Robotics* **2**, 1 (2024).
 - [10] F. Fischer, M. Jeong, and T. Qiu, Miniature magneto-oscillatory wireless sensor for magnetic field and gradient measurements, *Applied Physics Letters* **125**, 074102 (2024).
 - [11] B. Gleich, I. Schmale, T. Nielsen, and J. Rahmer, Miniature magneto-mechanical resonators for wireless tracking and sensing, *Science* **380**, 966 (2023).

- [12] B. Gleich, I. Schmale, T. Nielsen, and J. Rahmer, Miniature magneto-mechanical resonators for wireless tracking and sensing [supplementary material], *Science* **380**, 966 (2023).
- [13] C. C. Collins, Miniature passive pressure transensor for implanting in the eye, *IEEE transactions on biomedical engineering* **BME-14**, 74 (1967).
- [14] T. Merbach, F. Kexel, J. Faltinath, M. Möddel, M. Schlüter, T. Knopp, and F. Mohn, Wireless and passive pressure detection using magneto-mechanical resonances in process engineering (2025), [arXiv:2502.09575](https://arxiv.org/abs/2502.09575).
- [15] T. Knopp, F. Mohn, F. Foerger, F. Thieben, N. Hackelberg, J. Faltinath, A. Tsanda, M. Boberg, and M. Möddel, Empirical study of magnet distance on magneto-mechanical resonance frequency, *Current Directions in Biomedical Engineering* **10**, 377 (2024).
- [16] F. Mohn, F. Thieben, and T. Knopp, Low-cost analog signal chain for transmit-receive circuits of passive induction-based resonators (2025), [arXiv:2502.03202](https://arxiv.org/abs/2502.03202).
- [17] N. Hackelberg, J. Schumacher, M. Graeser, and T. Knopp, A flexible high-performance signal generation and digitization plattform based on low-cost hardware, *International Journal on Magnetic Particle Imaging* **8** (2022).
- [18] I. H. Grinberg, A. Mangu, C. W. Peterson, E. Wilken-Resman, J. T. Bernhard, and G. Bahl, Magnetostatic spring softening and stiffening in magneto-mechanical resonator systems, *IEEE Transactions on Magnetics* **55**, 1 (2019).
- [19] C. Li, A. Kanj, J. Jing, G. Bahl, and S. Tawfick, Pivot bearings for efficient torsional magneto-mechanical resonators (2024), [arXiv:2410.14855](https://arxiv.org/abs/2410.14855).
- [20] K. Levenberg, A method for the solution of certain nonlinear problems in least squares, *Quarterly of applied mathematics* **2**, 164 (1944).
- [21] B. F. Edwards, D. M. Riffe, J.-Y. Ji, and W. A. Booth, Interactions between uniformly magnetized spheres, *American Journal of Physics* **85**, 130 (2017).
- [22] A. J. Petruska and J. J. Abbott, Optimal permanent-magnet geometries for dipole field approximation, *IEEE Transactions on Magnetics* **49**, 811 (2013).